Transient Fault Parameters of DC-Excited Vernier Reluctance Synchronous Condenser

Mkhululi Mabhula, *Student Member*, *IEEE* and Maarten J. Kamper, *Senior Member*, *IEEE*
Department of Electrical and Electronic Engineering
Stellenbosch University
Stellenbosch, South Africa
mabhulamkhululi@gmail.com, kamper@sun.ac.za

***Abstract*—A brief evaluation of the behavior of a non-classical DC-excited reluctance synchronous machine parameters operating as a synchronous condenser is presented in this paper. The evaluation involves fault analysis of the machine under 3-phase short-circuit using the proposed accurate transient simulation methods. The transient current and reactance parameters are calculated under absorbing and generating reactive power operating conditions of the synchronous condenser. These parameters are compared under normal and fault conditions in which observations are used to explain how the machine provides grid strength under fault conditions.**

***Index Terms*—finite element, frozen permeability, inductance, symmetric fault, synchronous condenser, transient currents, two-axis modeling, wound field flux modulation machines**

I. Introduction

Traditional power generation is currently being replaced more and more with renewable energy-based power generation. With this power generation, the grid connection and grid power supply are mainly inverter based. However, with the growth in inverter-based supplies, the grid strength is weakened under fault conditions. To compensate for this, the industry has begun to use again, as in the past, grid connected synchronous condensers (SCs). SCs are ideal grid compensators because they provide reactive power, inertia and most important grid strength. Another advantage is that the ground surface footprint per MVAR of SCs is very small [1], [2].

However, the major disadvantage of SCs is that they require relatively much maintenance due to the rotating masses [3]. The bulk of this maintenance indeed lies in the wound rotor and in the rotating field exciter. To minimize this maintenance, the proposal to use the so-called flux switching machines as SCs was recently investigated [4]. In these types of electric machines, the salient pole rotor is passive with no copper windings but only laminated steel, and the field windings are mounted stationary on the stator. Hence the major disadvantage of a complicated rotor and rotating field exciter is solved. Furthermore, the simple rotor brings a great cost advantage.

As an alternative to the proposed flux switching machines, this paper looks at the DC-excited reluctance machine (DC-VRM) [5] as a SC. The DC-VRM is very similar to the flux switching machines but is simpler in the winding layout by using non-overlapping coils with short end-windings. The short end-windings of the stator distinguish this machine significantly from the classic SC machine with its long end-windings.

The authors would like to thank the Centre for Renewable and Sustainable Energy Studies (CRSES) of Stellenbosch University South Africa for financial support of this study.

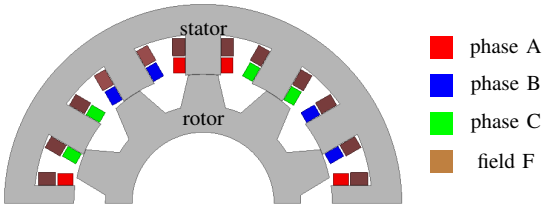

Fig. 1. Developed DC-VRM Ansys-Maxwell model for SC fault simulation results.

A very important and unanswered research question about the DC-VRM as SC is whether this type of SC does provide grid strength under fault conditions [6]. In this paper, this aspect of the DC-VRM as a SC is investigated. Note that the DC-VRM has no damper windings, so only the direct- (D), quadrature (Q)-, and field-(F) i.e. DQF, transient conditions are considered in the analysis. The paper concludes with the determination of the transient reactance of the DC-VRM SC, from which the grid strength provided by this SC is evaluated.

II. DC-VRM Specifications

Figure 1 shows the developed DC-VRM model in Ansys-Maxwell to be simulated under the defined fault conditions, as explained in Section III, when operating as SC. The important dimensions and winding parameter specifications are given in Table I. The machine's single, concentrated tooth coils results into low conduction losses, and reduced material and manufacturing costs. Also, the machine's only laminated rotor stack results into a robust rotor structure with high reliability.

III. SC Fault Definition

The fault analysis studied in this paper is the abnormal electrical machine and system behavior under conditions of symmetrical short-circuit (symmetrical 3-phase fault) [7]. Such conditions are accidentally caused in the system through insulation failure of equipment, or flash-over of lines initiated

TABLE I
DC-VRM DIMENSIONAL AND WINDING PARAMETERS

Parameters	Value	
stator outer, inner diameter	700.0, 454.9	mm
rotor inner diameter, stack length	250, 109.6	mm
stator, rotor slots	12, 10	
stator, field winding turns	69, 95	
rotor pole-pairing	0.8	

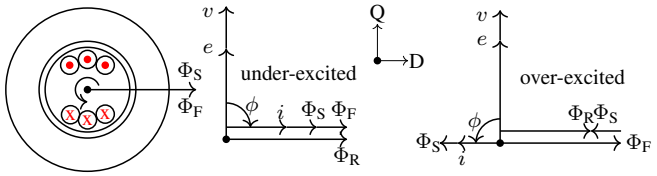

Fig. 2. Ideal SC phasor diagrams.

by a lightning stroke, or through accidental fault operation. The power system must be protected against short-circuit currents by disconnecting the fault part of the system by means of circuit breakers operated by protective relaying. Hence it is important to analyze the parameters (e.g., estimation of the current behavior and current magnitude under short-circuit condition) of the machine under fault conditions, which also is important for proper choice of circuit breakers and protective relays [1], [8]. Section IV explains the principle operation of the SC.

IV. DC-VRM IN SC MODE

In SC mode, the machine operates at no-load i.e., with a freely rotating shaft and with controlled field excitation. In this mode, variation of the excitation causes the machine to have a purely reactive stator current, lagging if under-excited and leading if over-excited as shown in Fig. 2. In Fig. 2, Φ_{R}, Φ_{S} and Φ_{F} are resultant excitation, stator and field flux respectively, e is the field excitation voltage and ϕ is the power factor angle.

When under-excited condition, when the DC field excitation is increased at no-load, the field excitation provides some of the required Φ_{R}, causing Φ_{S} to add as shown in Fig. 2, to produce the correct e. The machine is said to behave then as a lagging SC, i.e. the machine absorbs reactive power from the network. When over-excited, when the field is increased beyond its rated value, Φ_{S} counteracts the large Φ_{F} as shown in Fig. 2, to produce the fixed Φ_{R} and e in the SC. The machine is said to behave then as a leading SC, i.e. the machine supplies reactive power to the network [1].

V. SC MODELING

Adapting the DQ-axes machine model [3], the instantaneous DQ-axes stator voltages (v_{D}, v_{Q}) are related to the instantaneous 3-phase stator voltages (v_{A}, v_{B}, v_{C}) and electrical position θ of the axis of phase A as

$$\begin{aligned} v_{\mathrm{D}} &= \frac{2}{3}[v_{\mathrm{A}}\cos(\theta) + v_{\mathrm{B}}\cos(\theta-\beta) + v_{\mathrm{C}}\cos(\theta-2\beta)] \\ v_{\mathrm{Q}} &= \frac{-2}{3}[v_{\mathrm{A}}\sin(\theta) + v_{\mathrm{B}}\sin(\theta-\beta) + v_{\mathrm{C}}\sin(\theta-2\beta)], \end{aligned} \tag{1}$$

where $\beta = 2\pi/3$. With balanced 3-phase voltages and speed rotation ω corresponding to the frequency, the 3-phase voltages of (1) can be written as

$$\begin{aligned} v_{\mathrm{A}} &= v_{\mathrm{M}}\sin(\theta-\delta) \\ v_{\mathrm{B}} &= v_{\mathrm{M}}\sin(\theta-\delta-\beta) \\ v_{\mathrm{C}} &= v_{\mathrm{M}}\sin(\theta-\delta-2\beta). \end{aligned} \tag{2}$$

In (2), v_{M} is the voltage peak-value, position $\theta = 0$ corresponds to the coincidence of the axis of phase A with the rotor D-axis, and δ is the phase angle of the voltage phasor leading with respect to the Q-axis. Ideally in SC mode $\delta = 0$ as illustrated in Fig. 2.

Furthermore, the DQ-axes voltages of (1) and F-axis voltage (v_{F}) are expressed as [3]

$$\begin{aligned} v_{\mathrm{D}} &= r_{\mathrm{S}} i_{\mathrm{D}} + \dot{\lambda}_{\mathrm{D}} - \omega(\lambda_{\mathrm{E}} + \lambda_{\mathrm{Q}}) \\ v_{\mathrm{Q}} &= r_{\mathrm{S}} i_{\mathrm{Q}} + \dot{\lambda}_{\mathrm{Q}} + \omega(\lambda_{\mathrm{E}} + \lambda_{\mathrm{D}}) \\ v_{\mathrm{F}} &= r_{\mathrm{F}} i_{\mathrm{F}} + \dot{\lambda}_{\mathrm{F}} + \omega\lambda_{\mathrm{F}}, \end{aligned} \tag{3}$$

where r_{S}, r_F are the stator, field resistance and λ_{F}, λ_{E} (calculated from [9]) are the field and end-winding flux linkages respectively. The DQ-axes currents (i_{D}, i_{Q}) and flux linkages (λ_{D}, λ_{Q}) are respectively related to the stator phase currents i_{A}, i_{B}, i_{C} and flux linkages λ_{A}, λ_{B}, λ_{C} by expressions identical to (1). For the voltage-fed SC, to solve for the unknown parameters in (3), the current variables are considered to be dependent on the state-variable flux linkages. From (3), the state-variables are given by

$$\begin{aligned} \dot{\lambda}_{\mathrm{D}} &= v_{\mathrm{D}} - i_{\mathrm{D}} r_{\mathrm{S}} + \omega\lambda_{\mathrm{Q}} \\ \dot{\lambda}_{\mathrm{Q}} &= v_{\mathrm{Q}} - i_{\mathrm{Q}} r_{\mathrm{S}} - \omega\lambda_{\mathrm{D}} \\ \dot{\lambda}_{\mathrm{F}} &= v_{\mathrm{F}} - i_{\mathrm{F}} r_{\mathrm{F}} - \omega\lambda_{\mathrm{F}}. \end{aligned} \tag{4}$$

Thus, the stator and field current variables of the SC are solved from (4).

VI. STEADY-STATE INDUCTANCE CALCULATION AND REPRESENTATION

In order to analytically predict the current behavior and magnitude under the fault, the *steady-state* inductances must be determine from the time invariant (static) flux linkages of (3). To implement the latter, the solved steady-state stator and field current variables from (4) are used in conjunction with the frozen permeability method (FPM) [10] to segregate the flux linkages at an operating point defined by the DQF-axes currents. Thus, utilizing the FPM, the steady-state flux linkages

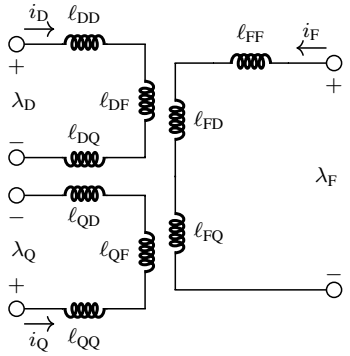

Fig. 3. DC-VRM DQF-axes inductance equivalent circuit representation.

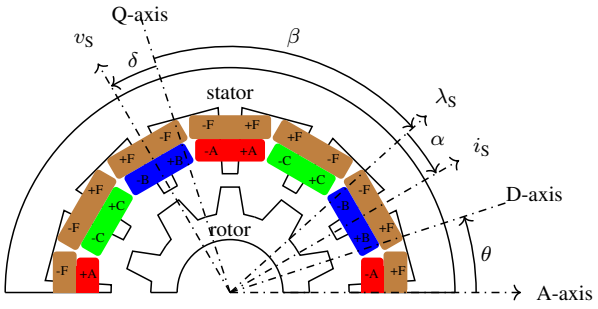

Fig. 4. DC-VRM cross-section and the position of the DQ-axes and voltage, flux linkage and current phasors at stead-state.

in (3) are segregated in terms of the DQF-axes inductances rising from the DQF-axes currents, respectively expressed as

$$\begin{aligned}\lambda_D &= (i_D\ell_{DD} + \ell_{DQ}i_Q + \ell_{DF}i_F)\\ \lambda_Q &= (i_D\ell_{QD} + \ell_{QQ}i_Q + \ell_{QF}i_F)\\ \lambda_F &= (i_D\ell_{FD} + \ell_{FQ}i_Q + \ell_{FF}i_F),\end{aligned} \tag{5}$$

where ℓ_{DD}, ℓ_{QQ}, ℓ_{DF}, ℓ_{FD}, ℓ_{FF} are the DQF-axes self inductances due to the i_D, i_Q, i_F currents respectively, and ℓ_{DQ}, ℓ_{QD}, ℓ_{QF}, ℓ_{FQ} are cross-axes inductances. Excluding end-winding effects, the SC can be virtually represented in a complete circuit form corresponding to the inductances of (5), aligned with each of the respective D, Q and F axes as shown in Fig. 3. Note, ideally the field coil are always a D-axis winding. The DQ-axes orientation on the DC-VRM cross-section with respect to the voltage, flux linkage and current phasors is shown in Fig. 4. Following Fig. 4, knowing the voltage $v_S\angle\delta$, the flux linkage $\lambda_S\angle-\beta$ and current $i_S\angle-(\beta+\alpha)$ can be solved using (3). Knowing the flux linkage and current, the steady-state inductances of (5) can then be simply but accurately calculated from (5) using FPM.

VII. SC Analytical Fault Current Calculation

To analytically estimate the fault currents of the SC, the calculated inductances of Section VI are used to compute the transient inductances and time constants [1], [3], [11], [12]. From [12], the transient D-axis self inductance (l'_{DD}) is determined first, from which the transient stator (T'_A) and field (T'_D) short-circuit time constants are then determined. The transient D-axis self inductance is given by [12]

$$\ell'_{DD} = (\ell_{DD} + \ell_E) - \frac{\ell_{DF}\ell_{FD}}{\ell_{FF}}, \tag{6}$$

where the inductances are defined from the flux linkages of (5). Also, the stator transient time constant is defined as [12]

$$T'_A = \frac{1}{r_S(\frac{1}{(\ell_{DD}+\ell_E)} + \frac{1}{\ell'_{DD}})}, \tag{7}$$

and the field transient time constant as

$$T'_D = \frac{(\ell_{FF} - \frac{\ell_{DF}\ell_{FD}}{(\ell_{DD}+\ell_E)})}{r_F}. \tag{8}$$

By defining the internal voltage as $e = \omega\ell_{DF}i_F$, the transient DQF currents after the short-circuit can be analytically approximated as [12]

$$\begin{aligned}i_D(t) \approxeq &-\frac{e}{\omega(\ell_{DD}+\ell_E)} - \dots\\ &\dots e(\frac{1}{\omega\ell'_{DD}} - \frac{1}{\omega(\ell_{DD}+\ell_E)})\exp(-\frac{1}{T'_D}) - \dots\\ &\dots \frac{e}{\omega\ell'_{DD}}\exp(-\frac{1}{T_A})\cos(\omega t),\end{aligned} \tag{9}$$

$$i_Q(t) \approxeq -\frac{e}{\omega\ell'_{QQ}}\exp(-\frac{1}{T_A})\sin(\omega t), \tag{10}$$

and

$$i_F(t) \approxeq e\{\frac{1}{\ell_{DF}} + \frac{\ell_{DF}}{\omega\ell_{FF}\ell'_{DD}}[\exp(-\frac{1}{T'_D}) - \exp(-\frac{1}{T_A})\cos(\omega t)]\}. \tag{11}$$

VIII. SC Fault Simulation Procedure

Simplorer-Maxwell in conjunction with Ansys-Maxwell (SA-M) [13] is used in the fault transient simulation procedure of the DC-VRM as a SC. The Ansys-Maxwell model is the 2D FE model shown in Fig. 1. The Simplorer-Maxwell is the model of power systems and power electronics connected to Ansys-Maxwell model. The main advantage of SA-M is, that it is possible to calculate directly the phase flux linkages that includes the higher space harmonics of the machine. The solutions for all 3-phase currents are then obtained, which are then transformed to DQF-axes similar to (1). Thus, apart from heavy demand upon computational time which comes with SA-M, SA-M is particularly useful for cases of unbalanced, whether steady-state or fault conditions.

Figure 5 shows the SA-M developed setup model for the simulation. Figure 6 shows the single-line power system diagram of Fig. 5, which comprises of a voltage source e_G, switches (S_0 and S_1) and the SC. In addition to the 3-phase short-circuit at time t_1 (when S_0 is open and S_1 closed), e_G, as a constant voltage source, supplies the SC before the short-circuit fault (when S_0 is closed and S_1 open).

It is important to state that when the fault occurs at t_1, the small impedance ($z_S = \sqrt{r_S + x_S}$) of the SC results in a very

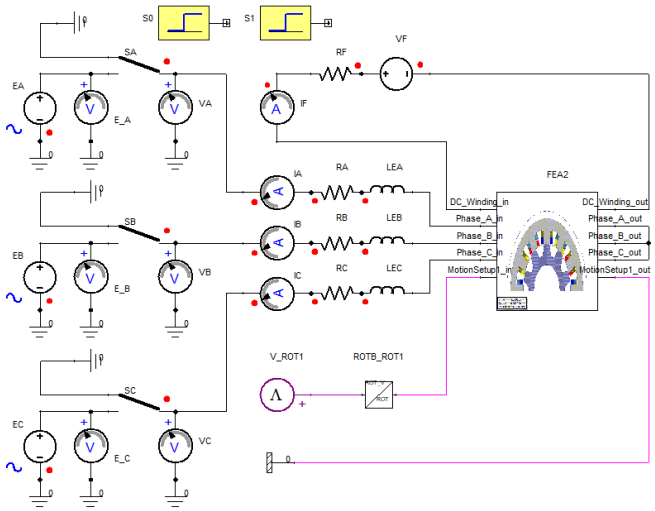

Fig. 5. Developed Simplorer/Ansys-Maxwell model for the SC fault simulation results.

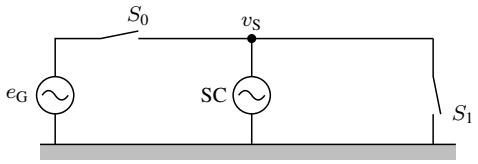

Fig. 6. Single-line power system diagram used for fault simulation representation.

high fault current which is limited only by this impedance. Thus, the fault current developed under transient conditions depend only on the resistance (r_S) and reactance (x_S).

Since in SC mode, i.e. at no-load ideally with $\delta = 0°$ (see Fig. 4), from (1) and (2), $v_D = 0$, $v_Q = 400(\sqrt{2/3})$ V at 50 Hz. This is set for the DQ-axes voltage supply in Fig. 5, i.e. Fig. 6. These supply voltages are necessary to bring the SC to steady-state between times $t_0 = 0$ s (when S_0 is closed and S_1 open) and $t_1 = 1$ s at the occurrence of the fault.

IX. SC Fault Simulation Results

Figures 7-9 show the current behavior of the DC-VRM before ($0.8 \leqslant t < t_1$) and after ($t_1 \leqslant t \leqslant 1.8$) the fault where $t_1 = 1$ s as discussed in Section VIII.

In Fig. 7, only phase A and field currents solved from (4) are shown for three operating points defined by the field current ($i_F = 0$, 1 and 2 pu). In this way the effect of different reactive power modes on the fault transient can be observed. It is important to state that even though Fig. 7 show only phase A currents, each phase appears to have a different magnitude immediately upon the fault, however, each obeying an exponential decay pattern from fault to steady-state. The latter is so because the point on the voltage wave at which the fault occurs is different for each phase. From Fig. 7, during the fault, the DC-VRM shows its characteristic time-varying behavior. Thus, in the event of the fault, the flux across the air gap of the DC-VRM undergoes dynamic change with

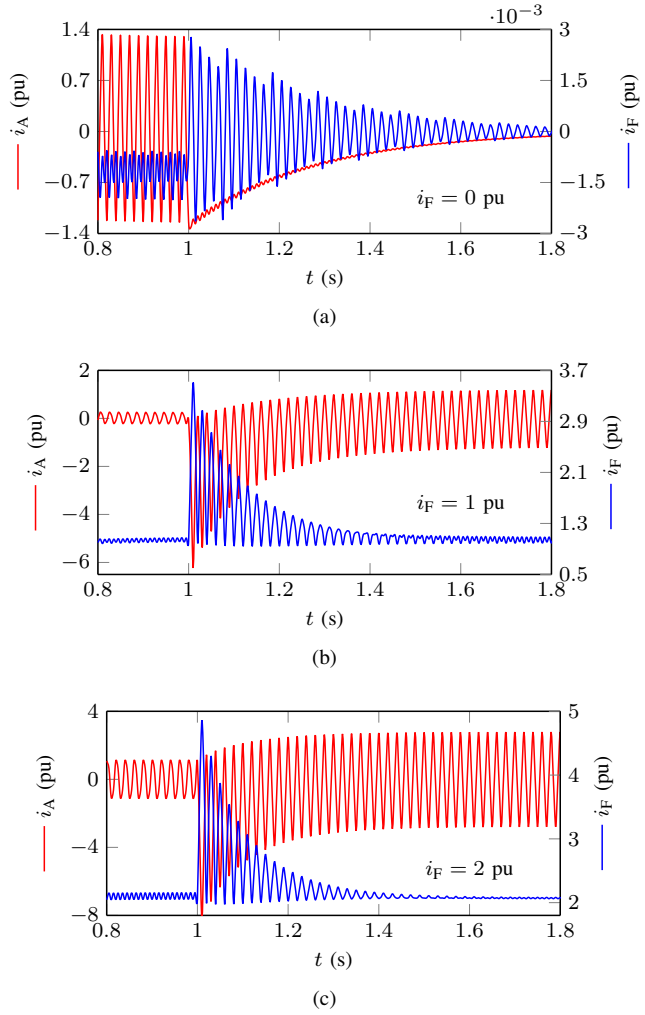

Fig. 7. Simulated current versus time of phase A and field windings before and after fault at $i_F =$ (a) 0 pu, (b) 1 pu and (c) 2 pu.

associated transients in the field windings. The short-circuit current decrease exponentially with time as the air-gap flux is much larger at the instant of the fault than few cycles later. As the air-gap flux reduces because of the limited field current capacity, the stator current decreases. When i_F is 1 and 2 pu in Fig. 7, the steady-state phase A current after the fault exist because of the field to the DC-VRM remains energized.

As stated in Section VII, the steady-state inductances of the machine before the fault are computed using the FPM (Section VI) to analytically estimate the DQF-axes currents. These steady-state average actual-inductances before the fault are given in Table II. The cross-coupling inductance parameters are calculated to be approximately zero. Also in Table II given are the calculated steady-state average actual-inductances after the fault ($t \geqslant 1.6$ s). The latter inductances are shown to be not equal to the inductances before the fault as classical textbooks assume. Using the actual-inductances given in Table II, Table III gives the calculated transient parameters of (6)-(8) before and after the fault. The currents of (9)-(11) are shown in Figs. 8 and 9 (blue lines) using the actual-inductances and transient

TABLE II
STEADY-STATE AVERAGE ACTUAL-INDUCTANCES CALCULATED USING FPM BEFORE AND AFTER THE FAULT

	*Before (**After) the fault		
i_F	0	1	2
ℓ_{DD}	0.085 (0.087)	0.084 (0.067)	0.052 (0.043)
ℓ_{DF}	0.106 (0.111)	0.106 (0.080)	0.055 (0.040)
ℓ_{QQ}	0.079 (0.081)	0.079 (0.074)	0.058 (0.054)
ℓ_{FF}	0.488 (0.496)	0.482 (0.422)	0.329 (0.297)
ℓ_{FD}	0.164 (0.166)	0.159 (0.120)	0.083 (0.060)
ℓ_E	0.00131		

* $0.8 \leqslant t < t_1$, ** $t \geqslant 1.6$.

TABLE III
CALCULATED TRANSIENT PARAMETERS BEFORE AND AFTER THE FAULT

	*Before (**After) the fault		
i_F	0	1	2
ℓ'_{DD}	0.052 (0.050)	0.052 (0.044)	0.045 (0.035)
T_A	0.192 (0.188)	0.189 (0.170)	0.162 (0.129)
T'_D	0.034 (0.190)	0.034 (0.1854)	0.029 (0.160)

* $0.8 \leqslant t < t_1$, ** $t \geqslant 1.6$.

parameters before the fault as given in Tables II and III. The red colored lines in Figs. 8 and 9 represent the SA-M solved currents.

From Figs. 8 and 9, it can be observed that the estimated analytic currents (blue lines) does not give a good representation of the SA-M simulated currents (red lines) during the first few cycles. However, a good prediction is observed during second part of the fault transient and in the steady-state condition, i.e. $t \geqslant 1.6$ s. To this end, it is a question if it is correct to assume that the steady-state actual-inductances before the fault, and henceforth transient parameters , do not change during the fault ($t \geqslant t_1$), which is an assumption in [12]. Thus, since (9)-(11) is an approximation as mentioned by [12], the transient condition is a very complex condition to describe accurately. The latter is extremely complex in the case of the DC-VRM, which is completely different from the conventional machine, i.e. with its double salient structure and the field winding stationary on the stator [5].

X. DC-VRM Grid Strength Support Under Fault

The per unit reactances of the DC-VRM as SC under grid fault conditions are summarized in Table IV and Fig. 10. These reactances are calculated from the steady-state actual-inductances in Table II, estimated either before or after the fault using FPM. What is interesting of these results is the effect the operating condition of the DV-VRM as SC has on the parameters. Nevertheless, per unit reactances of the given range in Table IV have been found for the DC-VRM under consideration. These are important data for the power utility. These parameter results together with the phase current waveforms of Fig. 7, are positive indicators of good strength the DC-VRM can provide as SC to the power grid [3].

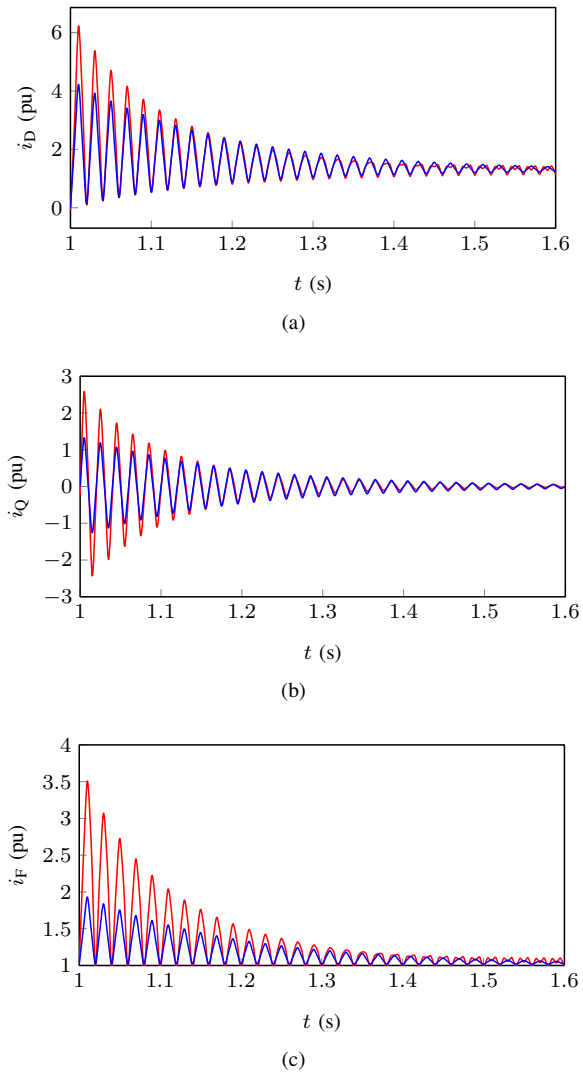

Fig. 8. SA-M simulated (red-lines) and estimated (blue-lines) (a) D-axis, (b) Q-axis and (c) F-axis fault currents at $i_F = 1$ pu.

TABLE IV
PER UNIT DC-VRM REACTANCES BEFORE AND AFTER THE FAULT

	*Before (**After) the fault			Range
i_F	0	1	2	0 – 2
x_{DD}	0.996 (1.022)	0.988 (0.793)	0.608 (0.502)	0.50-1.00
x_{QQ}	0.942 (0.951)	0.927 (0.876)	0.676 (0.638)	0.64-0.95
x'_{DD}	0.580 (0.587)	0.577 (0.523)	0.444 (0.406)	0.41-0.59

* $0.8 \leqslant t < t_1$, ** $t \geqslant 1.6$.

XI. Further Studies

It is critical to take note that even though the DC-VRM does not have damper windings as in wound-field synchronous machines (WF-SMs), the SA-M simulated results of Figs. 8 and 9 show that the DC-VRM has inherent subtransient components in its fault current [3], which are not included in (9)-(11). The subtransient parameters (i.e. ℓ''_{DD}, T''_D) are important in determining the initial peak currents when the fault occurs. Incorporating the additional subtransient terms

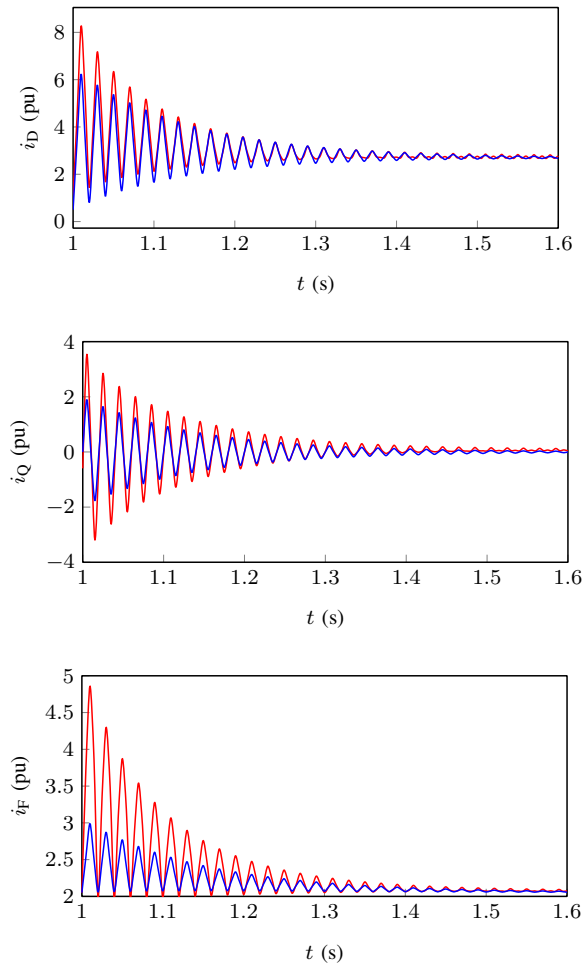

Fig. 9. SA-M simulated (red-lines) and estimated (blue-lines) (a) D-axis, (b) Q-axis and (c) F-axis fault currents at $i_F = 2$ pu.

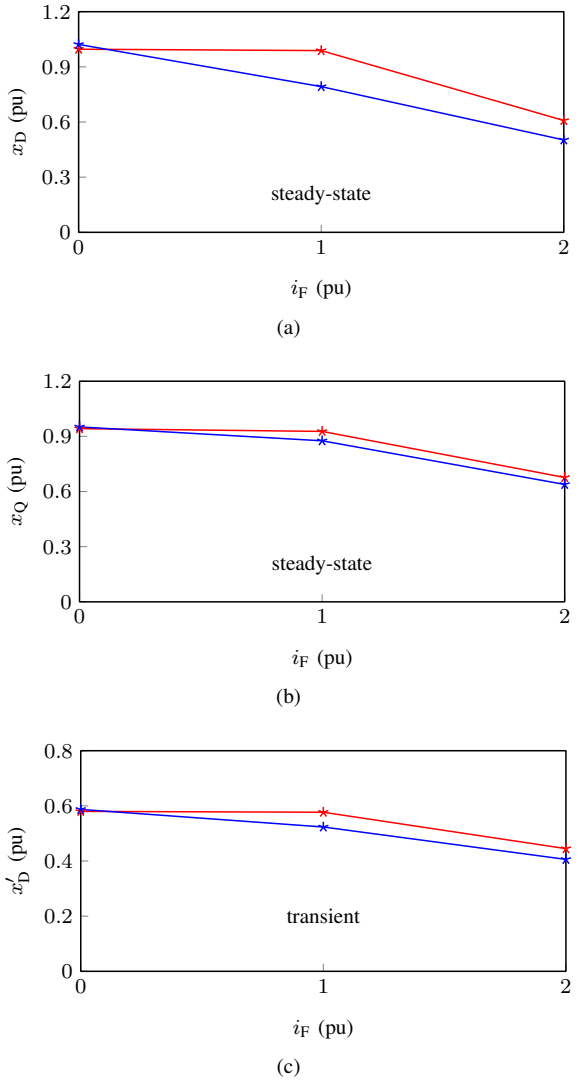

Fig. 10. Actual (a) x_D, (b) x_Q and transient (c) x'_D reactances before (red markers) and after (blue markers) fault.

in (9)-(11) may even double the initial peak current [3], [11], which may explain the differences in the results of Figs. 8 and 9.

For permanent magnet synchronous machines (PM-SMs), [14] considers the damping circuit due to the magnet and retaining ring eddy-currents as the subtransient circuits. Deriving analytical expressions for the subtransient parameters in this case is fairly simple as the magnets and retaining ring are well defined. However, in the case of the DC-VRM, this is much complex. Hence, in this study the subtransient parameters are estimated as functions of the transient parameters before the fault. Table V gives the subtransient parameters values where $x''_{DD} = 0.8x'_{DD}$, $x''_{QQ} = 0.6x'_{QQ}$ and $T''_D = 0.4T'_D$. With these incorporated in the analytical expression of [12] with damper windings, Fig. 11 shows now a much better estimation of the transient D-axis current, for example, of the DC-VRM. The latter is also done for QF-axes currents using $x''_{QQ} = 0.5x'_{QQ}$ and good results are obtained.

Having that said, one can argue that subtransient currents are not possible in the DC-VRM as there is no subtranseint circuits. In this way, to get better results, ℓ_{DD} and ℓ_{DF} are

TABLE V
SUBTRANSIENT, TRANSIENT AND MODIFIED-TRANSIENT ESTIMATED PARAMETERS OF THE DC-VRM AT $i_F = 2$ PU

Subtransient			**Transient**			**Modified-transient**		
x''_{DD}	:	0.36	x'_{DD}	:	0.44	x'_{DD}	:	0.76
x''_{QQ}	:	0.40	x'_{QQ}	:	0.67	x'_{QQ}	:	0.67
T''_D	:	0.06	T'_D	:	0.16	T'_D	:	0.14
T_{dlr}	:	0.13	–	:	–	–	:	–

respectively altered by a factor of 1.6 and 2 in order to modify the transient parameters ℓ'_{DD} and T'_D. This is under the assumption that the transient parameters of Table IV are somehow under estimated since a strong initial peak current response is observed. The latter could be due to the field winding circuit experiencing a significant induced electromagnetic force from the phase winding magneto motive force harmonics fields [15]. The modified-transient parameters are given in Table V. Using modified-transient parameters, better representation of

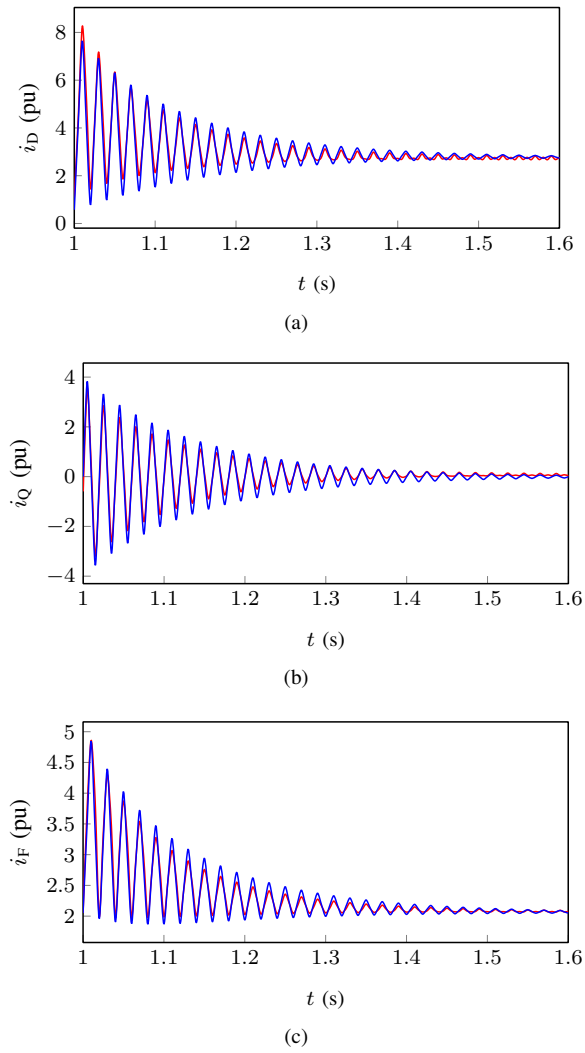

Fig. 11. SA-M simulated (red-line) and subtransient + transient estimated (blue-line) (a) D-axis, (b) Q-axis and (c) F-axis fault currents at $i_F = 2$.

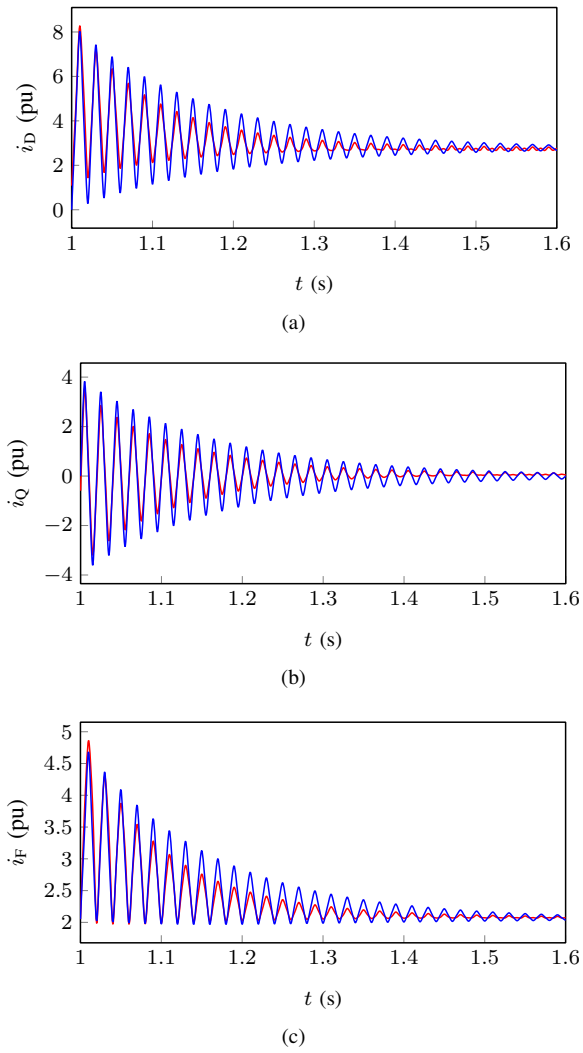

Fig. 12. SA-M simulated (red-line) and modified-transient estimated (blue-line) (a) D-axis, (b) Q-axis and (c) F-axis fault currents at $i_F = 2$.

the initial SA-M simulated currents are obtained as shown in Fig. 12. However, a slow damping with the modified-transient parameters is now observed as shown in Fig. 12.

XII. Conclusions

In this paper, the development and application of models and classical equations necessary to evaluate and estimate the DC-VRM transient parameter behavior under fault conditions, are presented. This is important in order to provide some answers to questions on the DC-VRM's performance as SC under fault conditions. The below given conclusions are drawn from the results of this paper.

The SA-M simulated results of the studied DC-VRM as SC show that the machine supplies $4-6$ pu current under 3-phase short circuit faults. This is a positive indication of the good grid strength the DC-VRM can provide as SC.

By using accurate calculated steady-state inductances of the DC-VRM using the FPM, classical transient equations show to predict accurately the transient fault currents of the machine under different field operating conditions of SC. However, it is found that the initial peak currents of the DC-VRM are far under estimated by using this method.

Together with the above, it is observed that the DC-VRM inherent a strong subtransient response with fast damping. Using approximations of subtransient parameters, good estimations of subtransient and transient fault currents are obtained.

In another way to find good fault current prediction the subtransient response was discarded, and a modified-transient approach was followed. With modified-transient parameters, good estimations of the initial fault currents are obtained, however with not as good, slow damping transient response prediction.

From the investigation per unit transient reactances of the DC-VRM of between 0.44 to 0.58 pu for the D-axis and 0.67 to 0.95 pu for the Q-axis are found. The latter depends on the operating conditions of the machine as SC at the time of the fault. If subtransient modeling is assumed, subtransient DQ-axis reactances of between 0.36 to 0.4 pu are found for the

DC-VRM as SC.

REFERENCES

[1] D. Kothari and I. Nagrath, *Modern Power System Analysis*, 3rd ed. Tata McGraw-Hill Publishing Company, 2003.

[2] D. Mooney and B. Kroposki, "Electricity, resources, and building systems integration at the national renewable energy laboratory," in *2009 IEEE Power Energy Society General Meeting*, 2009, pp. 1–3.

[3] M. Say, *Alternating Current Machines*, 5th ed., ser. Longman scientific and technical. Longman Scientific & Technical, 1986.

[4] U. B. Akuru, M. J. Kamper, and M. Mabhula, "Optimisation and design performance of a small-scale dc vernier reluctance machine for direct-drive wind generator drives," in *2020 IEEE Energy Conversion Congress and Exposition (ECCE)*, 2020, pp. 2965–2970.

[5] S. Jia, R. Qu, J. Li, and D. Li, "Principles of stator dc winding excited vernier reluctance machines," *IEEE Transactions on Energy Conversion*, vol. 31, no. 3, pp. 935–946, 2016.

[6] Y. Liu, R. Yu, L. Zhang, D. Jiang, N. Chen, and D. Zhao, "Research on short-circuit currents calculation method considering dynamic reactive power support of renewable energy systems," in *2018 2nd IEEE Conference on Energy Internet and Energy System Integration (EI2)*, 2018, pp. 1–9.

[7] P. Janiga, Z. Eleschova, and D. Viglas, "Short-circuit - analysis and calculation," *WSEAS Transactions on Power Systems*, vol. 9, pp. 291–299, September 2014.

[8] J. Glover, M. Sarma, and T. Overbye, *Power System Analysis and Design*. Cengage Learning, 2011.

[9] J. H. J. Potgieter and M. J. Kamper, "Calculation methods and effects of end-winding inductance and permanent-magnet end flux on performance prediction of nonoverlap winding permanent-magnet machines," *IEEE Transactions on Industry Applications*, vol. 50, no. 4, pp. 2458–2466, 2014.

[10] Z. Li, Y. Chen, X. Huang, X. Li, W. Ying, B. Shen, L. Wu, Y. Fang, and T. Long, "Dynamic modeling of surface-mounted permanent magnet motors considering saturation," in *2019 IEEE Energy Conversion Congress and Exposition (ECCE)*, 2019, pp. 5624–5628.

[11] American Nations Standard Institute, *IEEE Recommendation for: Calculating Short-Circuit Currents in Industrial and Commercial Power Systems, IEEE Std 551*. Institute of Electrical and Electronic Engineerings, Inc, 2006.

[12] T. A. Lipo, *Analysis of synchronous machines*. CRC Press, June 2012.

[13] "Ansys Maxwell Low Frequency Electromagnetic Field Simulation," https://www.ansys.com/products/electronics/ansys-maxwell, Accessed: 20 January 2021.

[14] K. W. Klontz, T. J. E. Miller, M. I. McGilp, H. Karmaker, and P. Zhong, "Short-circuit analysis of permanent-magnet generators," *IEEE Transactions on Industry Applications*, vol. 47, no. 4, pp. 1670–1680, 2011.

[15] X. Sun, Z. Q. Zhu, S. Cai, L. Wang, F. R. Wei, and B. Shao, "Influence of stator slot and rotor pole number combination on field winding induced voltage ripple in hybrid excitation switched flux machine," *IEEE Transactions on Energy Conversion*, vol. 36, no. 2, pp. 1245–1261, 2021.